

# The Effect of Discharge Pulse Energy in Electrospray Deposition of Amorphous Coatings

A. A. Burkov\*

*Institute of Materials Science, Khabarovsk Scientific Center, Far East Branch, Russian Academy of Sciences, Khabarovsk, 680042 Russia*

*\*e-mail: burkovalex@mail.ru*

Received July 20, 2021; revised May 30, 2022; accepted June 6, 2022

**Abstract**—This paper presents the results of studying an amorphous coating on a steel 35 substrate prepared by electrospray deposition in a mixture of iron granules with CBCrSiMoW powder. A prolonged duration of discharges increased the iron concentration in the composition of the coatings, decreasing a fraction of the amorphous phase from 67 to 50 vol %. The amorphous coating had a resistance to oxidation at a temperature of 700°C that was 23 times higher than did steel 35. Polarization tests of samples in a 3.5% NaCl solution showed an increase in the corrosion current density with increasing pulse duration above 200  $\mu$ s. The microhardness of the coatings ranged from 399 to 759 HV. The average wear rate of the coatings under dry sliding conditions ranged from  $1.6 \times 10^{-6}$  to  $10.9 \times 10^{-6}$  mm<sup>3</sup>/Nm, which is from 4 to 22 times lower than that of uncoated steel 35. The coating obtained with the longest pulses exhibited the highest friction coefficient and wear rate due to the lowest concentration of the amorphous phase. The results suggested that, to ensure sufficient coating thickness and an acceptable concentration of the amorphous phase, the optimal duration of the discharge pulses should range from 50 to 200  $\mu$ s.

**Keywords:** Fe-based metal glasses, coatings, electrospray alloying, corrosion resistance, heat resistance, wear

**DOI:** 10.1134/S2070205122050057

## 1. INTRODUCTION

Metallic glasses (MGs) are amorphous metallic materials with improved magnetic, electrochemical, tribological, and catalytic properties [1–4], as well as radiation resistance, biocompatibility, and noncytotoxicity [5–7]. Iron-based MG coatings attract the attention of researchers and engineers because they improve the hardness, heat resistance, and corrosion resistance of steel products [8, 9]. Various technologies are used to obtain MG coatings, such as magnetron sputtering, laser cladding, plasma sputtering, electroplating, and electrospray alloying (ESA) [10–15]. ESA is based on the transfer of the anode material to the cathode surface under the action of many short ( $\sim 10^{-4}$  s) electric discharges. Of the above methods, ESA is characterized by the smallest thermal effect on the substrate material; it does not require expensive equipment and vacuum maintenance. The resulting coatings are favorably distinguished by high adhesion to the substrate due to the metallurgical bond between the coating and the substrate [15–18].

The ESA process is typically performed using units equipped with a manual electrode holder. The possibility of automated ESA using a mixture of powders of metals (W, Mo, Cr) and nonmetals (Si, C, SiB<sub>4</sub>) to deposit amorphous coatings with an anode from iron

granules was demonstrated [19]. Iron granules and a steel substrate acted as a source of iron for metallic glasses. When the discharge passes between the granule and the substrate, the powder electrostatically fixed on its surface is introduced into the melt microbath. This is accompanied by the convective and diffusive mixing of elements to a homogeneous state. The high cooling rate of the material after the termination of the discharge, up to  $10^5$ – $10^6$  K/s, results in the fixation of an amorphous structure from a multicomponent melt with high glass-forming ability. The discharge energy can affect the cooling conditions of the material during ESA [17]. Therefore, this work is aimed at studying the effect of the duration of discharge pulses on the structure and properties of amorphous coatings obtained by electrospray treatment of steel 35 in a mixture of iron granules with a multicomponent powder.

## 2. EXPERIMENTAL

Coatings were deposited on a substrate made of steel 35 in the form of a cylinder 12 mm in diameter and 10 mm in height. The material to be deposited was a powder mixture (Table 1) and granules of low-alloy steel St. 3.

**Table 1.** Composition of the powder mixture

Powder	at %	Element	at %
Si	5.91	Si	15.27
C	3.49	C	24.03
Mo	20.02	Mo	10.00
Cr	21.7	Cr	19.99
SiB <sub>4</sub>	7.66	B	20.60
WC	41.23	W	10.09

Granules were obtained by cutting a wire  $4 \pm 0.2$  mm in diameter into cylinders  $4 \pm 0.2$  mm high. The initial powders had a purity of at least 99.5 wt %. The powder mixture was prepared by mixing the powders in a PM-400 planetary ball mill for 90 min under argon at 250 rpm for 2 h. According to the data of the Sorbi-M instrument, the resulting powder had a specific surface area of  $3.1 \text{ m}^2/\text{g}$ . The dried powder was added to the iron granules at a concentration of 9 vol %, and all the system was loaded into a steel container. The layout of the installation for coating is shown in Fig. 1a. The substrate was placed in the center of the container. The container was installed at an angle of  $45^\circ$  and connected to the drive.

The container was rotated at 60 rpm. The substrate was fixed on a steel rod switched to the negative terminal of the pulse generator and connected to a drive that rotates it in the direction opposite to the container at a speed of 60 rpm. The positive terminal of the generator was connected to the container through copper brushes. An IMES-40 pulse generator produced rectangular current pulses with an amplitude of  $110 \pm 10$  A

at a voltage of  $30 \pm 5$  V, duration  $\tau$  in the range of 20–500  $\mu\text{s}$ , and a frequency of 1000 Hz (Table 2). Argon was fed into the container at a rate of  $10 \text{ L min}^{-1}$  to prevent oxidation processes on the surface of the samples. The deposition time for each coating was 360 s.

The phase composition of the samples was studied using a DRON-7 X-ray diffractometer in  $\text{CuK}\alpha$  radiation. The composition of the coatings was studied using a Sigma 300 VP scanning electron microscope (SEM) equipped with an INCA Energy spectrum analyzer. Raman microspectrometry was performed using an InVia Reflex instrument (Renishaw, United Kingdom). The probe parameters were a 532-nm laser and an output power of 5 mW at 500 repetitions. Electrochemical polarization tests were carried out in a 3.5% NaCl solution in a standard three-electrode cell using a P-2X potentiostat. A conventional silver–silver chloride electrode was used as a reference electrode. A platinum foil served as a counterelectrode, and coated samples and steel 35 were used as a working electrode. The contact area of the samples with the electrolyte was  $1 \text{ cm}^2$ . Scanning was carried out at a potential sweep rate of 3 mV/s in the range of  $-1.5$  to  $0.5$  V. Five repetitive measurements were made for each sample to ensure the reproducibility of the results. Tests for resistance to high-temperature oxidation were carried out in a muffle furnace at a temperature of  $700^\circ\text{C}$  in air. The total testing time was 100 h. The hardness of the coatings was measured using a PMT-3M microhardness tester at a load of 0.5 N using the Vickers method. The wear resistance of the coatings was studied according to *ASTM G99-17* with dry sliding friction at a speed of 0.47 m/s under loads of 10 and 25 N using a disk made of M45 high-speed steel with a hardness of

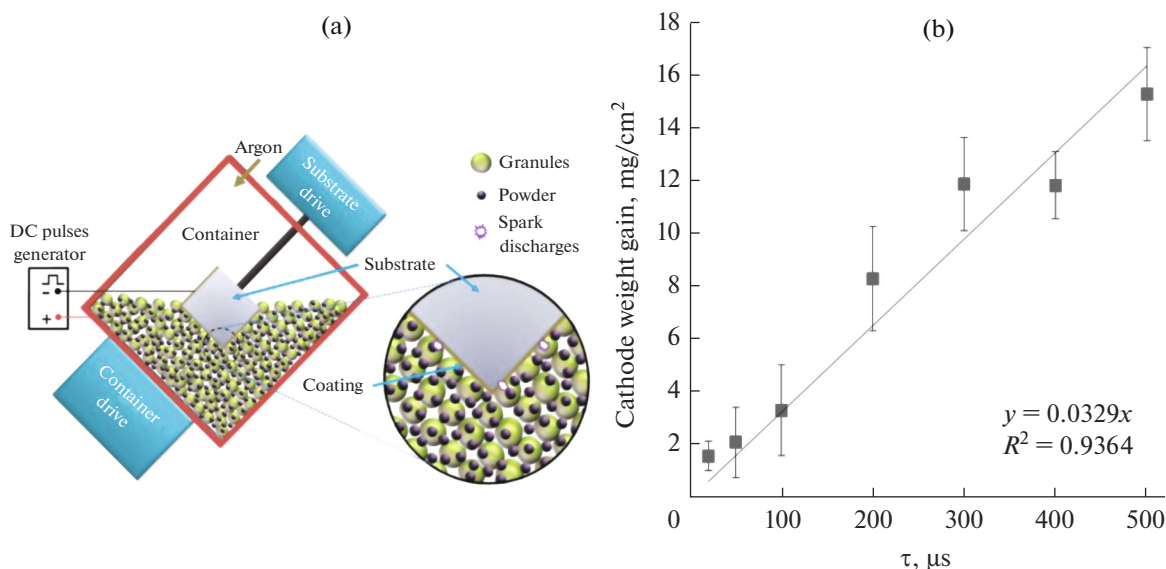


**Fig. 1.** (a) Schematic diagram of electrospark alloying in granules with the addition of powder. (b) Weight gain of the substrate depending on the pulse duration after 6 min of ESA.

**Table 2.** Electrospark deposition parameters, designation of coatings, and their thickness

Coating	Pulse duration, $\mu\text{s}$	Energy, J	Thickness, $\mu\text{m}$
C20	20	0.066	$22 \pm 9$
C50	50	0.165	$29 \pm 5$
C100	100	0.33	$38 \pm 9$
C200	200	0.66	$39 \pm 7$
C300	300	0.99	$47 \pm 17$
C400	400	1.32	$54 \pm 9$
C500	500	1.65	$56 \pm 17$

60 HRC as a counterbody. The change in the weight of the samples was monitored using a balance with a sensitivity of 0.1 mg.

### 3. RESULTS AND DISCUSSION

During the electrospark deposition of coatings in a mixture of steel granules and CrMoWCBSi powder, the weight of the substrates increased because of the deposition of the material of the granules and powder onto the cathode (Fig. 1b). With an increase in the duration of the pulses sent by the generator, the average weight gain of the cathode increased monotonically by almost ten times from 1.6 to 15.4 mg/cm<sup>2</sup> in 6 min of deposition. Weight gain of the cathode  $\Delta m_c$  during ESA in granules can be expressed as the sum of the weights of the material of the granules  $\Delta m_a$  and powder  $\Delta m_p$  transferred to the melt microbath (MB) on the cathode surface minus cathode erosion  $\epsilon_c$ ,

$$\Delta m_c = \Delta m_a + \Delta m_p - \epsilon_c.$$

The value of  $\Delta m_a$  increases with an increase in the discharge energy during ESA [20]. In this case, an increase in the weight gain of the cathode occurs due to an increase in anode erosion  $\Delta m_a$  and powder fixation  $\Delta m_p$ . The value of  $\Delta m_p$  is the mass of powder fixed by the forces of electrostatic attraction on the surface of the electrodes, equal to the melt microbath area.

Backscattered electron SEM images and the distribution of elements in the cross section of the coatings are shown in Fig. 2. The average thickness of the coatings increased from 22 to 56  $\mu\text{m}$  with the increasing duration of the discharge pulses (Table 2). A small number of pores and transverse cracks were observed in the microstructure of the coatings. The occurrence of transverse cracks is usually explained by the difference between the coefficients of thermal expansion of the coating and the substrate [21, 22]. Light inclusions in coatings less than 15  $\mu\text{m}$  in diameter are tungsten carbide and metallic molybdenum, which do not have time to dissolve in the metal melt due to their high melting temperature (Figs. 3a, 3b). In the layers of the substrate adjacent to the coating, light spots are visi-

ble, which are the heat-affected zones. SEM images suggest that the thickness of the heat-affected zone did not exceed 30  $\mu\text{m}$ . Thus, we can conclude that the ESA has a weak thermal effect on the substrate.

The energy-dispersive spectroscopy (EDS) of the coatings showed a uniform distribution of elements in the cross section of the coatings (Figs. 2b, 2d, 2f). The EDS data for the coating surface showed that prolongation in  $\tau$  in the range from 20 to 500  $\mu\text{s}$  increased the iron concentration in the coatings from 50 to 67 at % with a simultaneous decrease in the concentration of elements of the CrMoWCBSi powder (Fig. 3c). This is explained by the fact that a larger amount of iron is drawn into the discharge microbath from the granules and the substrate during a prolonged discharge time. During the passage of the discharge, the powder fixed on the electrode surface, which was equal to the melt microbath, melted and mixed with the electrode material, forming a coating. Thus, the amount of powder transferred to the coating in one discharge depends on the diameter of the melt microbath. The dependence of the microbath diameter at the cathode on  $\tau$  in the range from 20 to 500  $\mu\text{s}$  is well described by a logarithmic dependence: at low  $\tau$  (20–100  $\mu\text{s}$ ), the diameter of the melting region increased strongly, and it increased slightly at  $\tau$  above 100  $\mu\text{s}$  [23]. At  $\tau$  more than 100  $\mu\text{s}$ , the amount of powder in the microbath remains practically unchanged. At the same time, with an increase in  $\tau$  from 100 to 500  $\mu\text{s}$ , the depth of melt penetration of the substrate in the zone of action of the discharge increased, and, accordingly, the concentration of iron in the microbath grew. This explains the observed decrease in the concentration of powder elements in the coating with  $\tau$  above 100  $\mu\text{s}$ .

The results of X-ray phase analysis of the initial powder mixture and C100 coating are shown in Fig. 5. Reflections of tungsten carbide, molybdenum, chromium, silicon, and graphite were observed in the X-ray spectrum of the CrMoWCBSi powder (Fig. 4a).

The diffraction pattern of the coating shows a characteristic halo in the range of angles  $2\theta = 35^\circ\text{--}55^\circ$ , indicating the presence of an amorphous phase. Narrow Bragg reflections were also observed in the spectra

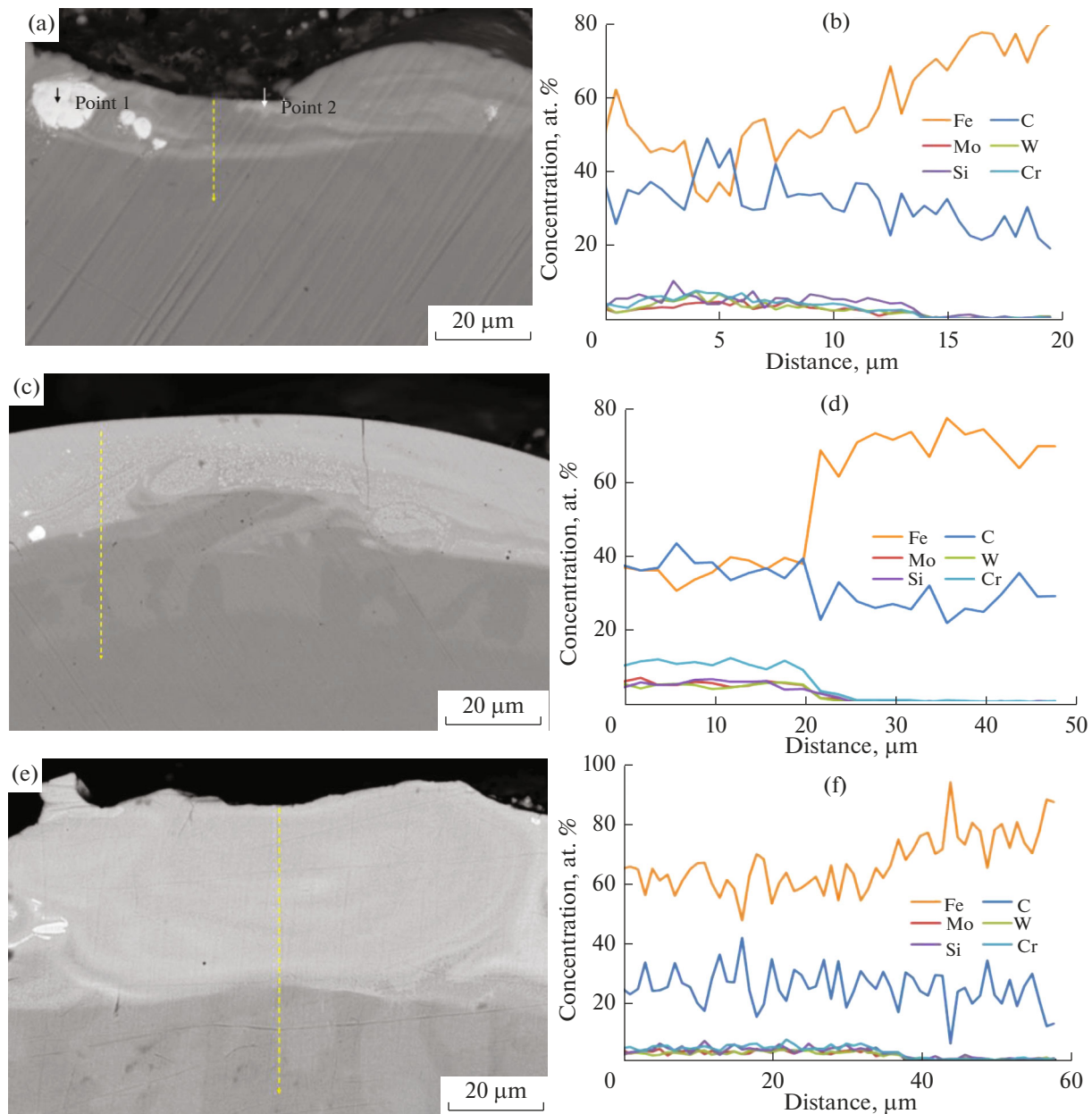


**Fig. 2.** (a, c, e) SEM images and (b, d, f) results of EDS scanning of the cross section of coatings (a, b) C20, (c, d) C100, and (e, f) C500. The dashed line indicates the scan area.

of the coatings, corresponding to  $\alpha$ Fe from the substrate, as well as to tungsten carbide and molybdenum. The presence of WC and Mo phases in the coatings is consistent with the SEM and EDS data (Figs. 2a, 3a, 3b) and is explained by their high melting points. The proportion of the amorphous phase, according to X-ray diffraction analysis, is usually calculated as the ratio of the sum of halo areas to the sum of halo areas and sharp Bragg reflections [24, 25],

$$V_{\text{Amor}} = \frac{\Sigma A_{\text{Amor}}}{\Sigma A_{\text{Amor}} + \Sigma A_{\text{Cryst}}},$$

where  $V_{\text{amor}}$  is the volume fraction of the amorphous phase and  $A_{\text{cryst}}$  and  $A_{\text{amor}}$  are the areas of crystalline reflections and amorphous halos, respectively. The calculation suggests that the fraction of the amorphous phase in the coatings ranged from 50 to 67 vol % (Fig. 4b). The largest fraction of the amorphous phase was observed in the coatings obtained at low  $\tau$ . This can be explained by the action of two factors: glass-forming ability and cooling rate. First, as the pulse duration increases, the coatings become enriched in iron (Fig. 3c), which decreases their glass-forming ability. Second, with a decrease in  $\tau$ , the velocity of the

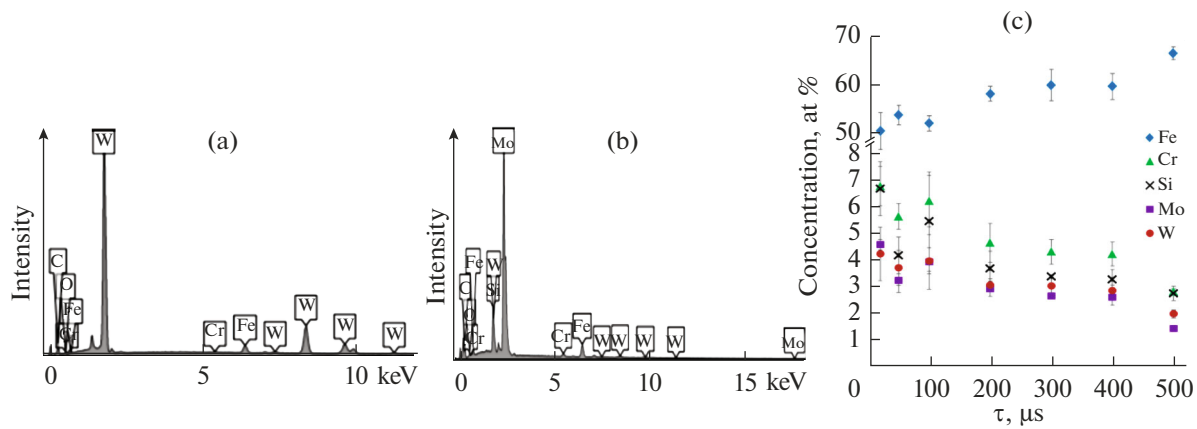


**Fig. 3.** EDS analysis of the coating regions at points (a) 1 and (b) 2 in Fig. 2a. (c) Concentrations of metals and silicon according to the EDS data of the coating surface as a function of  $\tau$ .

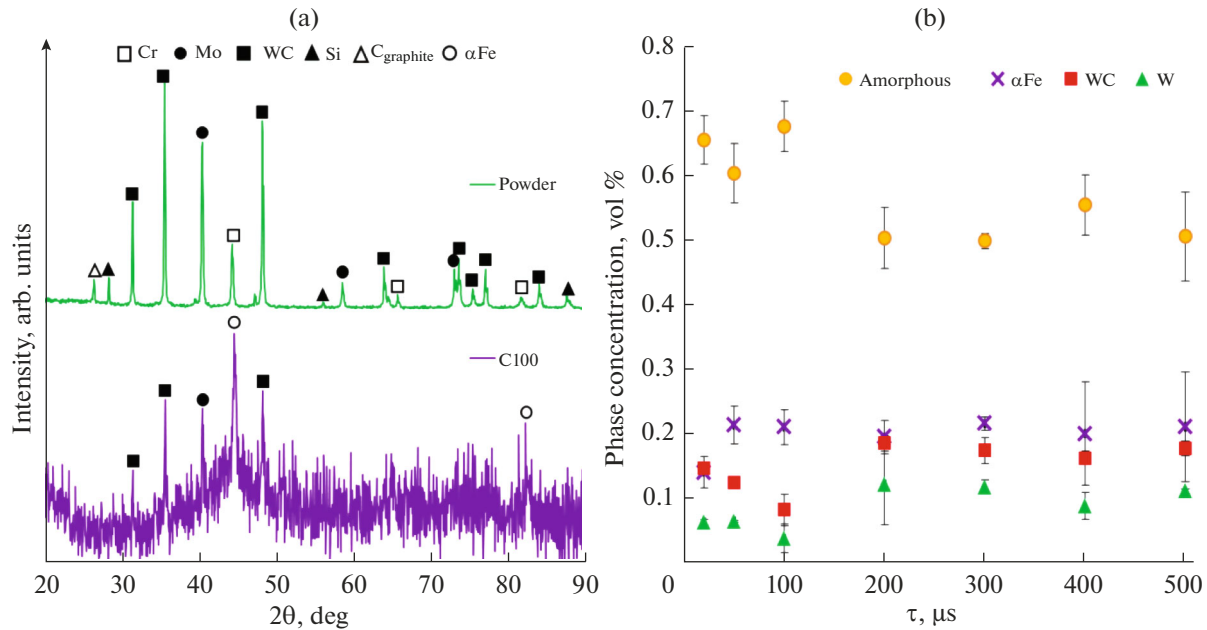


**Fig. 4.** (a) X-ray diffraction patterns of the multicomponent powder and C100 coating. (b) Phase composition of the deposited coatings according to XRD data.

solidification front in the melt microbath after the completion of the discharge increases, since the volumetric heating of the substrate is lower.

Potentiodynamic polarization tests were carried out in a 3.5% NaCl aqueous solution to study the corrosion resistance of steel 35 with MG coatings (Fig. 5a). Corrosion current density  $I_{\text{corr}}$ , corrosion potential  $E_{\text{corr}}$ , and polarization resistance  $R_p$  were calculated by extrapolating cathodic and anodic Tafel slopes using the Stern–Geary method (Table 3). The results of testing the coatings showed a decrease in the corrosion potential by 19–43% and in the current density by up to 2.17 times and an increase in the polariza-

tion resistance up to 6.9 times compared to steel 35. These changes can be explained by the amorphous structure of the coatings [26, 27]. Chromium, silicon, and tungsten, which are parts of amorphous coatings, can further improve their corrosion properties in a 3.5% NaCl solution [28]. This is due to the barrier properties of oxide films formed on the surface of the coating upon interaction with the electrolyte. As  $\tau$  increased from 200 to 500  $\mu\text{s}$ ,  $E_{\text{corr}}$  decreased and  $I_{\text{corr}}$  increased. The C500 coating showed the highest corrosion current and the lowest  $E_{\text{corr}}$  and  $R_p$  values. This is explained by an increase in the iron concentration in coatings with increasing  $\tau$ , since the corrosion resis-

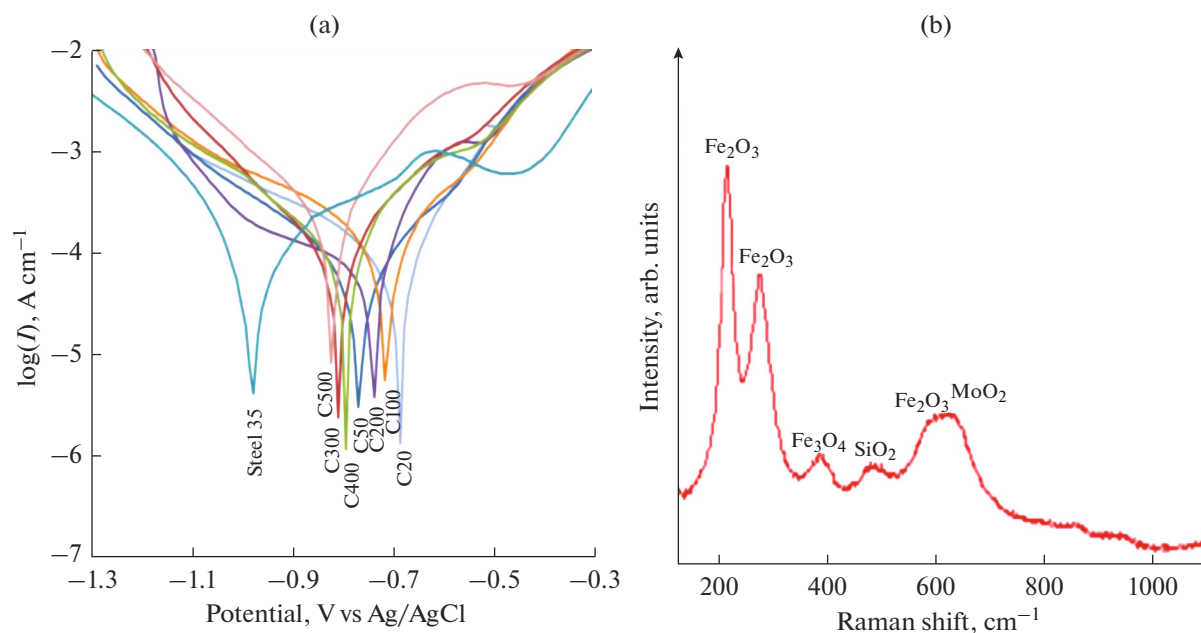


**Fig. 5.** (a) Polarization curves of steel 35 and amorphous coatings in a 3.5% NaCl solution. (b) Raman spectrum of the C100 surface after testing.

tance of amorphous nanocrystalline composites deteriorates with a decrease in the concentration of the amorphous phase [29].

Raman spectroscopy of the surface of the C100 coating after polarization testing showed the presence of  $\text{Fe}_2\text{O}_3$  (217, 279, and  $597\text{ cm}^{-1}$ ) along with a small amount of  $\text{Fe}_3\text{O}_4$  ( $390\text{ cm}^{-1}$ ),  $\text{SiO}_2$  ( $479\text{ cm}^{-1}$ ), and  $\text{MoO}_2$  ( $660\text{ cm}^{-1}$ ), which are insoluble corrosion products of the amorphous phase during tests in a 3.5% NaCl solution (Fig. 5b).

Figure 6a shows the kinetics of change in the weight of sample C100 and steel 35 at a temperature of  $700^\circ\text{C}$  in air. During 100 h of testing, the coated sample underwent oxidation 23 times less than steel 35 due to the limited contact of oxygen with the substrate. A section of the X-ray spectrum of the C100 coating after the heat resistance test (Fig. 6b) proves that the growth of the sample is due to the fixation of oxygen on the surface of the sample in the form of iron(III) oxide in the modification of hematite. In addition to hematite,  $\alpha\text{Fe}$  reflections were observed in the diffraction pat-

tern, which indicates a small thickness of the oxide layer through which X-rays penetrate. Raman spectroscopy of the oxide layer also showed the presence of  $\text{Fe}_2\text{O}_3$  (216, 279, and  $592\text{ cm}^{-1}$ ) (Fig. 6c). Magnetite  $\text{Fe}_3\text{O}_4$  ( $390\text{ cm}^{-1}$ ) is also observed together with a small amount of  $\text{SiO}_2$  ( $485\text{ cm}^{-1}$ ).  $\text{SiO}_2$  indicates corrosion of the amorphous phase during high-temperature oxidation. Silicon plays a significant role in the high heat resistance of MG coatings as silicon oxide has high barrier properties [30, 31].

The image of the cross section of the C100 coating after the heat-resistance test shows that the oxide layer is formed fragmentarily on the steel substrate in the thinnest places of the coating (Fig. 7a). The micrograph of a coating fragment (Fig. 7b) shows that the oxide layer continues to grow under the coating and in the most iron-rich regions of the coating.

The oxide layer does not form on top of the coating, which confirms the high resistance to oxidation of the formed amorphous layer. The EDS data show a significantly lower concentration of Cr, Mo, and Si in

**Table 3.** Corrosion parameters of samples

Parameter	Steel 35	C20	C50	C100	C200	C300	C400	C500
$E_{\text{corr}}$ , V	-0.98	-0.68	-0.77	-0.71	-0.74	-0.81	-0.79	-0.82
$I_{\text{corr}}$ , $\mu\text{A cm}^{-2}$	121.8	85.0	56.1	76.1	60.6	98.5	111.1	171.7
$R_p$ , $\text{k}\Omega$	14.8	38.7	89.8	49.2	46.9	76.9	101.9	31.2

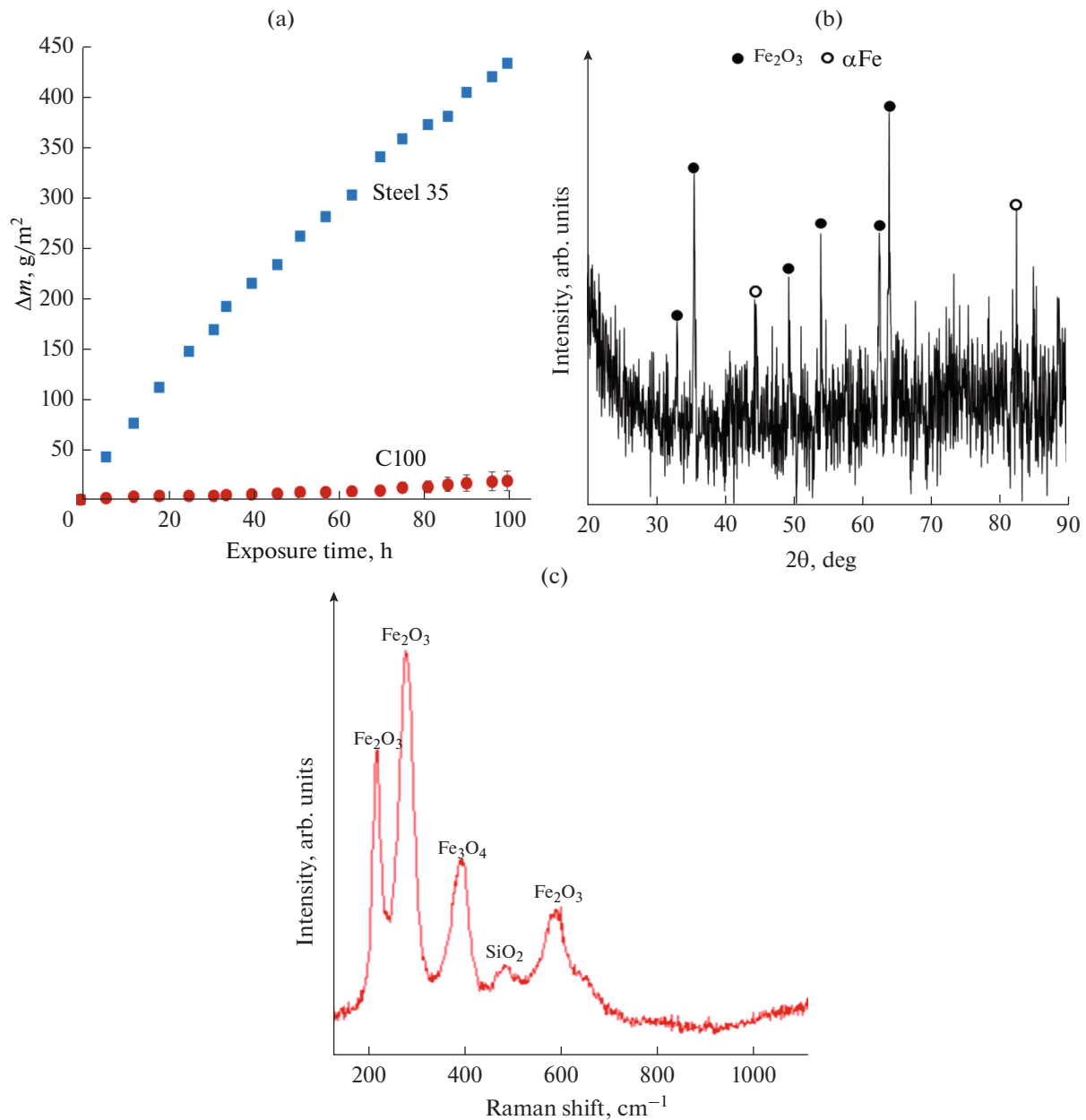


**Fig. 6.** (a) Cyclic heat resistance of C100 coating compared to steel 35 at 700°C. (b) X-ray diffraction pattern and (c) Raman spectra of the C100 coating surface after a heat-resistance test.

comparison with Fe in the oxide layer (Fig. 7d). This means little participation of the coating material in the formation of scale. Significantly, thin transverse cracks in the coating do not cause oxidation sites, as is shown in Fig. 7c.

Tests of the coatings for microhardness showed that for most of the samples, the average hardness values were in the range from 617 to 759 HV (Fig. 8a). In general, there was a tendency for the coating hardness to decrease with increasing  $\tau$ . The average hardness of the C500 coating was 399 HV. According to the published data, the hardness of most Fe-based metallic

glasses is 430 to 1200 HV [32–44]. Thus, the hardness of the developed coatings corresponds to the metallic glasses of similar composition.

The average values of the friction coefficient of the coatings ranged from 0.67 to 0.94 at a load of 25 N and from 0.62 to 0.69 at 70 N (Figs. 8b, 8c). The obtained values are within the range of friction coefficients for most MG coatings on a steel substrate. For most coatings, the friction coefficient was 15–25% lower than for steel 35. Under both loads, the highest friction coefficient was observed for the C500 coating. This

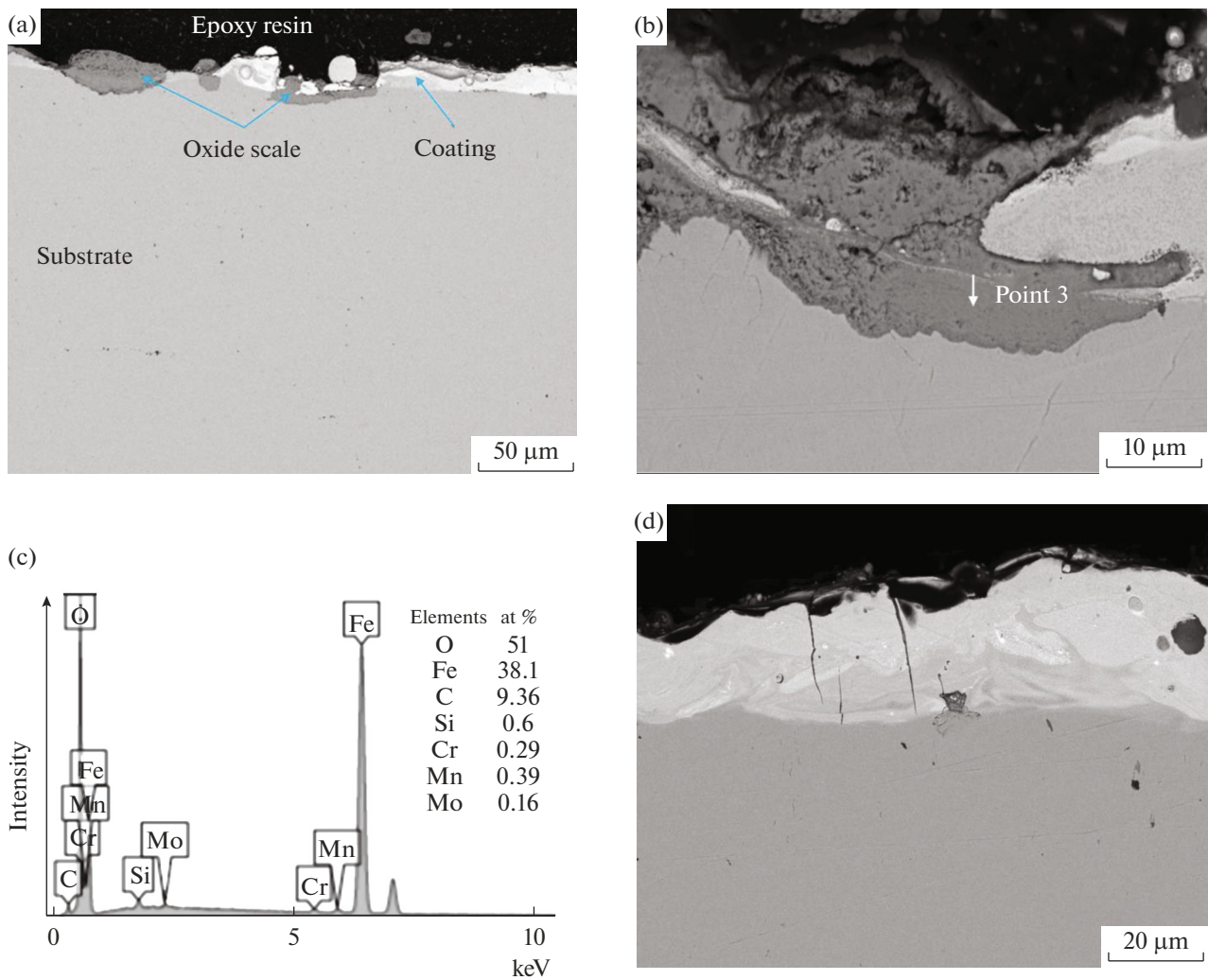


**Fig. 7.** SEM image of the cross section of the C100 coating after the cyclic oxidation test at magnification (a) 250 $\times$ , (b) 2500 $\times$ , and (d) 1200 $\times$ ; (c) EDS spectrum of point 3 (Fig. 7b).

can be explained by the low hardness of this coating due to the high iron concentration.

Testing the coatings for wear at loads of 25 and 70 N (Fig. 8d) yielded the average wear rate of coatings in the range of  $1.6 \times 10^{-6}$  to  $10.9 \times 10^{-6} \text{ mm}^3/(\text{N m})$ . The C20 coating applied at the lowest  $\tau$  showed a relatively high wear rate, which can be explained by its small thickness, which caused it to wear out quickly. The highest wear rate was observed for the C500 coating under both loads. This is due to the high concentration of iron in its composition and low hardness. The wear rate of C50–C400 coatings had similar values in the range from  $1.6 \times 10^{-6}$  to  $3 \times 10^{-6} \text{ mm}^3/(\text{N m})$  at a load of 25 N and from  $3.6 \times 10^{-6}$  to  $4.7 \times 10^{-6} \text{ mm}^3/(\text{N m})$  at 70 N. The protective effect of coatings is defined as the ratio of the wear rate of the substrate material to the wear rate of the coating. The protective effect of the prepared ESA coatings was in the range of 4 to 22

(Fig. 8d). Based on recent data [32–44], the dry slip wear rate of the presented MG coatings was in a wide range of  $2.7 \times 10^{-6}$ – $373 \times 10^{-6} \text{ mm}^3/(\text{N m})$ , and the protective effect is from 0.54 to 6. Thus, the data on the wear resistance of the obtained amorphous coatings are among the best among the previously published results.

## CONCLUSIONS

An amorphous coating was prepared on steel 35 by a new method of electrospark deposition in a mixture of iron granules with CBCrSiMoW powder. It is found that the amorphous phase predominates in the coating structure. With an increase in the duration of the discharge pulse, the fraction of the amorphous phase in the composition of the coatings decreased from 67 to 50 vol %. This is associated with the deterioration of



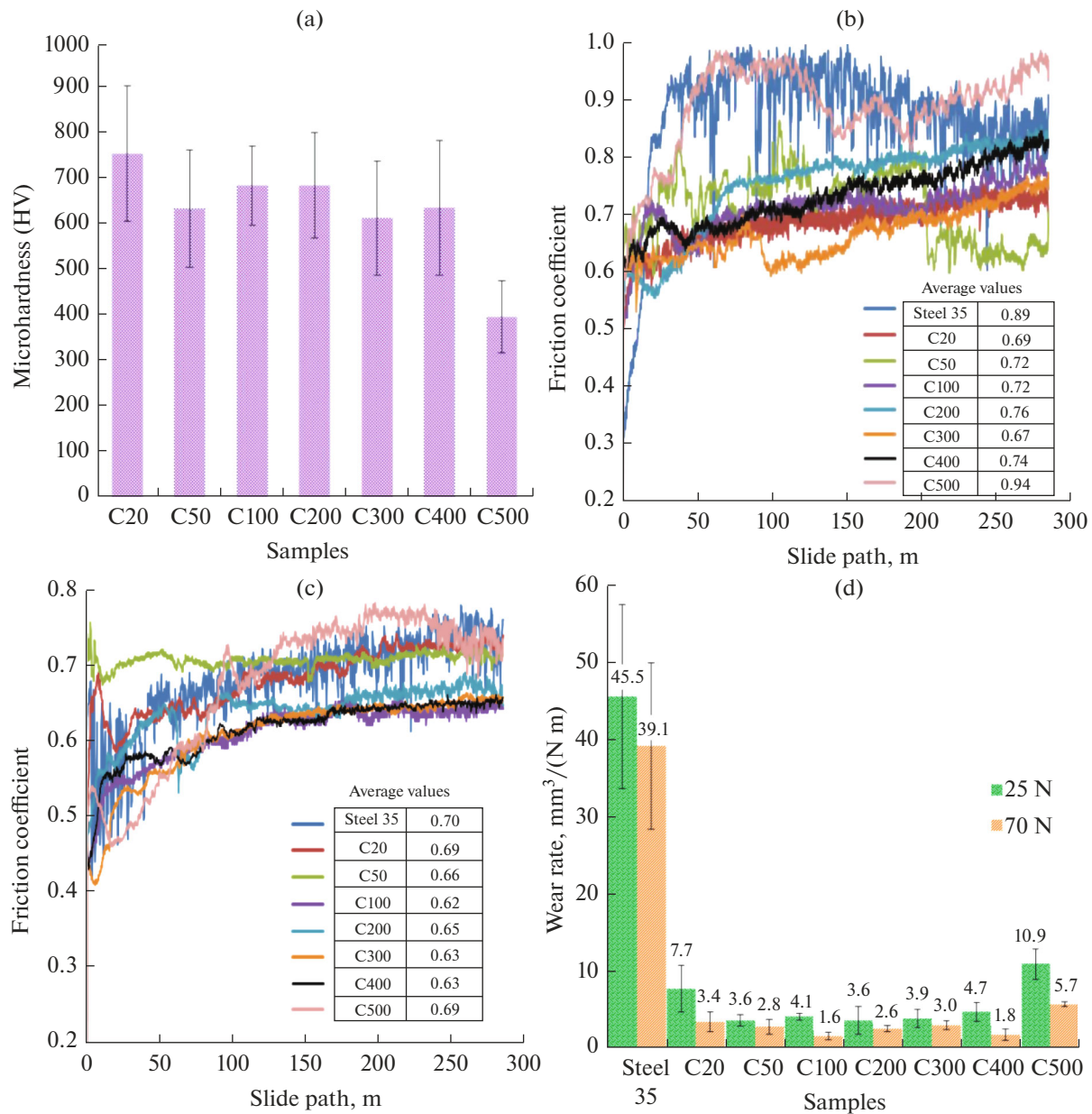


**Fig. 8.** (a) Dependence of microhardness of coatings on pulse duration; coefficient of friction of the coatings at loads of (b) 25 and (c) 70 N; (d) wear of the coatings in comparison with steel 35.

the glass-forming ability of the coating material due to iron enrichment and a decrease in the cooling rate of the material due to volumetric heating of the substrate. The deposited coating is characterized by high resistance to oxidation at a temperature of 700°C. Oxide scale formed fragmentarily on the steel substrate in the most iron-rich regions of the coating and was not detected on the coating surface. The microhardness of the coatings ranged from 399 to 759 HV. The average friction coefficient of the coatings ranged from 0.62 to 0.94. The average wear rate of the coatings was from  $1.6 \times 10^{-6}$  to  $10.9 \times 10^{-6}$  mm<sup>3</sup>/(N m), which is 4–22 times lower than that of steel 35. The coating

obtained with the longest pulses had the lowest hardness and wear resistance and the highest coefficient of friction due to the low concentration of the amorphous phase.

#### CONFLICT OF INTEREST

The authors declare that they have no conflicts of interest.

#### REFERENCES

- Masood, A., Belova, L., and Ström, V., *J. Magn. Magn. Mater.*, 2020, vol. 504, p. 166667.

2. Cherkezova-Zheleva, Z., et al., *Hyperfine Interact.*, 2020, vol. 241, no. 1, p. 1.
3. Ji, L., et al., *J. Phys. Chem. Solids*, 2020, vol. 145, p. 109546.
4. Zhang, Q., et al., *J. Mater. Sci. Technol.*, 2021, vol. 61, p. 159.
5. Suo, Y., et al., *Fusion Eng. Des.*, 2020, vol. 157, p. 111635.
6. Schroers, J., et al., *JOM*, 2009, vol. 61, no. 9, p. 21.
7. Wang, Y.B., et al., *Mater. Sci. Eng., C*, 2012, vol. 32, no. 3, p. 599.
8. Ibrahim, M.Z., et al., *Surf. Coat. Technol.*, 2020, vol. 392, p. 125755.
9. Wang, H., et al., *Mater. Chem. Phys.*, 2020, vol. 250, p. 123091.
10. Lee, J., Liou, M.L., and Duh, J.G., *Surf. Coat. Technol.*, 2017, vol. 310, p. 214.
11. Koga, Y., et al., *Mater. Trans.*, 2017, vol. 58, no. 10, p. 1444.
12. Chen, W.Y., et al., *Surf. Coat. Technol.*, 2020, vol. 389, p. 125636.
13. Burkov, A.A., Zaitsev, A.V., Syui, A.V., Zaikova, E.R., and Kaminskii, O.I., *Prot. Met. Phys. Chem. Surf.*, 2019, vol. 55, no. 1, p. 102.
14. Burkov, A.A. and Kulik, M.A., *Prot. Met. Phys. Chem. Surf.*, 2020, vol. 56, no. 6, p. 1217.
15. Cadney, S. and Brochu, M., *Intermetallics*, 2008, vol. 16, no. 4, p. 518.
16. Nikolenko, S.V. and Syui, N.A., *Prot. Met. Phys. Chem. Surf.*, 2017, vol. 53, no. 5, p. 889.
17. Felix, L.M., Kwan, C.C.F., and Zhou, N.Y., *Metall. Mater. Trans. A*, 2019, vol. 50, no. 9, p. 4223.
18. Kayali, Y. and Talas, S., *Prot. Met. Phys. Chem. Surf.*, 2021, vol. 57, p. 106.
19. Burkov, A.A., *Obrabotka Metallov (Tekhnologiya, Oborudovanie, Instrumenty)*, 2019, vol. 21, no. 4, p. 19.
20. Ribalko, A.V. and Sahin, O., *Surf. Coat. Technol.*, 2006, vol. 201, nos. 3–4, p. 1724.
21. Zhang, J., et al., *Trans. China Weld. Inst.*, 2009, vol. 30, no. 12, p. 17.
22. Salmaliyan, M. and Ghaeni, F.M., *Surf. Coat. Technol.*, 2017, vol. 321, p. 81.
23. Pyachin, S.A., et al., *Russ. Phys. J.*, 2019, vol. 61, no. 12, p. 2236.
24. Shkodich, N.F., et al., *J. Alloys Compd.*, 2018, vol. 741, p. 575.
25. Cheng, J., et al., *J. Alloys Compd.*, 2017, vol. 716, p. 88.
26. Guo, R.Q., et al., *Corros. Sci.*, 2011, vol. 53, no. 7, p. 2351.
27. Li, S., et al., *Mater. Sci. Eng., C*, 2015, vol. 52, p. 235.
28. Sagasti, A., Lopes, A.C., Lasheras, A., et al., *AIP Adv.*, 2018, vol. 8, p. 047702.
29. Coimbrao, D.D., Zepon, G., Koga, G.Y., et al., *J. Alloys Compd.*, 2020, vol. 826, p. 154123.
30. Garip, Y. and Ozdemir, O., *J. Alloys Compd.*, 2019, vol. 780.
31. Matsushita, J.-I., Satsukawa, T., Iwamoto, N., Wang, X.L., et al., *Mater. Sci. Forum*, 2016, vol. 868, p. 38.
32. Wang, G., et al., *J. Iron Steel Res. Int.*, 2016, vol. 23, no. 7, p. 699.
33. Hong, W.U., et al., *Trans. Nonferrous Met. Soc. China*, 2016, vol. 26, no. 6, p. 1629.
34. Paul, T., et al., *Lasers in Manufacturing and Materials Processing*, 2015, vol. 2, no. 4, p. 231.
35. Zhang, H., et al., *J. Non-Cryst. Solids*, 2014, vol. 406, p. 37.
36. Liu, L. and Zhang, C., *Thin Solid Films*, 2014, vol. 561, p. 70.
37. An, Y., et al., *Vacuum*, 2014, vol. 107, p. 132.
38. Yugeswaran, S., et al., *J. Alloys Compd.*, 2013, vol. 551, p. 168.
39. Zhang, C., et al., *Intermetallics*, 2012, vol. 29, p. 80.
40. Guo, R.Q., et al., *Intermetallics*, 2012, vol. 30, p. 94.
41. Li, X., et al., *J. Non-Cryst. Solids*, 2020, vol. 537, p. 120018.
42. Nayak, S.K., et al., *J. Alloys Compd.*, 2020, vol. 825, p. 154120.
43. Liang, D., et al., *Surf. Coat. Technol.*, 2020, vol. 387, p. 125535.
44. Ji, X., et al., *Wear*, 2019, vol. 438, p. 203113.

Translated by O. Zhukova